Computer Methods in Applied Mechanics and Engineering 427 (2024) 117030

Contents lists available at ScienceDirect

Comput. Methods Appl. Mech. Engrg.

journal homepage: www.elsevier.com/locate/cma

A phase-field model for the brittle fracture of Euler–Bernoulli beams coupling stretching and bending

Giovanni Corsi [a], Antonino Favata [b,*], Stefano Vidoli [b]

[a] BioRobotics Institute, Sant'Anna School of Advanced Studies, Pisa, Italy
[b] Department of Structural and Geotechnical Engineering, Sapienza University of Rome, Rome, Italy

ARTICLE INFO

Keywords:
Euler–Bernoulli beam
Fracture
Phase field

ABSTRACT

Damage gradient models seek to simulate fracture mechanics by modulating the material stiffness. Within this framework, a singular scalar field representing damage is commonly utilized to globally decrease elastic energy. However, when considering structural models like beams and plates, this approach often fails to adequately capture important aspects due to the interaction between stretching and bending contributions. In this work, we propose a model for planar Euler–Bernoulli beams that incorporates the following features: firstly, we utilize two phase-field damage parameters to describe material damaging, specifically addressing the 'erosion' occurring above and below the original, undamaged beam; secondly, we assume a simple linear dependence of the axial stress field on the thickness coordinate, along with linear dependence on the axial force and bending moment. By appropriately identifying the constitutive response, our model effectively considers the coupling between stretching and bending induced during through-the-thickness damage, demonstrating good agreement with 2D observations.

1. Introduction

In the realm of solid mechanics, a significant advancement in modeling brittle fracture has been the development of the Griffith theory within a variational framework [1] and its regularization using the Ambrosio–Tortorelli results [2] to create so-called "phase-field" gradient models [3,4]. These models are founded on the minimization of an energy functional that depends on both the displacement and damage fields. The damage field, denoted as α, is introduced to approximate the sharp crack discontinuity in a region exhibiting a smooth transition between undamaged ($\alpha = 0$) and fully broken material ($\alpha = 1$). A detailed exploration of the extensive literature in this domain falls beyond the scope of this paper, but interested readers can refer to comprehensive reviews on the subject (e.g., [5]).

Specifically, within this framework, the energy functional to be minimized is expressed as:

$$\mathcal{E}(\mathbf{u},\alpha) = \frac{1}{2}\int_{\Omega} \mathbb{C}(\alpha)\mathbf{E}(\mathbf{u})\cdot\mathbf{E}(\mathbf{u})\,\mathrm{d}\mathbf{x} + G_c\int_{\Omega}\left(\frac{(1-\alpha)^2}{4\delta} + \delta|\nabla\alpha|^2\right)\mathrm{d}\mathbf{x}, \tag{1}$$

Here, $\mathbf{u}$ represents the displacement field, $\mathbf{E}(\mathbf{u})$ corresponds to the strain field, $\mathbb{C}(\alpha)$ characterizes the elastic tensor, modulated by the phase-field α, $\delta > 0$ is a parameter controlling the width of the transition zone of α, and G_c is the fracture toughness. Typically, the elasticity tensor is assumed to be a multiplicative function of the form $\mathbb{C}(\alpha) = m(\alpha)\mathbb{C}_o$. When the modulation function $m(\alpha)$ is chosen

* Corresponding author.
E-mail address: antonino.favata@uniroma1.it (A. Favata).

https://doi.org/10.1016/j.cma.2024.117030
Received 24 February 2024; Received in revised form 19 April 2024; Accepted 25 April 2024

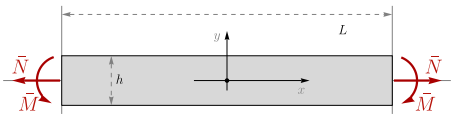

Fig. 1. Planar beam-like body subjected to axial forces $\bar{N}$ and bending moments $\bar{M}$.

as $(1-\alpha)^2$ and δ approaches zero, it has been demonstrated that the functional (1) approximates, in the sense of Γ-convergence, the energy functional of the Griffith theory of brittle fracture.

In the existing body of literature, various methodologies have been employed to model fracture in shells, plates, and beams. These methods encompass mesh-free techniques (e.g., [6–8]), XFEM (Extended Finite Element Method) approaches (e.g., [9–11]), and more. However an adaptation of the variational approach in the spirit of [3,4] is still lacking and it is aim of our present work.

1.1. Analytical and numerical results in 3D

We consider a prismatic beam-like body whose reference domain is shown in Fig. 1. It is characterized by a length L, a width b, a thickness $h \ll L$ and it is parametrized by the coordinates (x, y). For sake of simplicity we limit ourselves to planar deformations. The two opposite bases are subjected to the axial forces $\bar{N}$ and to the bending moments $\bar{M}$.

For a linear elastic isotropic material, the Saint-Venant solution assures that, far from the bases, the stress tensor has only one non-vanishing component given by

$$\boldsymbol{S} = S_{xx}\,\mathbf{a}_x \otimes \mathbf{a}_x, \quad S_{xx} = \frac{\bar{N}}{bh} + 12\,y\frac{\bar{M}}{bh^3}, \tag{2}$$

being $\mathbf{a}_x$ the direction of the beam axis. Now, let us suppose the material to be brittle and capable of sustaining arbitrarily large compressive stresses but finite stresses under tension: $-\infty < S_{xx} \le \sigma_c$. Some questions arise: (1) How is the elastic domain characterized? (2) What are the maximum sustainable loads in terms of $\bar{N}$ and $\bar{M}$?

We could solve analytically this problem considering that, since the stress distribution is linear through the thickness, its maximum value is reached at $y = h/2$ or at $y = -h/2$ for respectively positive or negative bending moments. Hence, the elastic domain is given by the intersection of the two regions

$$\frac{\bar{N}}{bh} + 6\,\frac{\bar{M}}{bh^2} \le \sigma_c \quad \text{and} \quad \frac{\bar{N}}{bh} - 6\,\frac{\bar{M}}{bh^2} \le \sigma_c. \tag{3}$$

This elastic domain is shown as light gray shaded area within the (N, M) plane in Fig. 2.

One can actually compute the same elastic domain using a standard damage-gradient model as the one discussed in the introduction. Indeed, minimization of the functional (1) with respect to $\boldsymbol{u}$ and α yields the Saint-Venant solution as unique global minimum until $S_{xx} \le \sigma_c$ in any point of the domain. However, this equilibrium branch becomes unstable when the stress reaches its critical value; stable branches are then characterized by localization of the damage field α in strips having thickness proportional to the parameter ℓ. Every localization strip where $\alpha \to 1$ simulate the material fracture. The results of such simulations are reported in Fig. 2 as color points and are in perfect agreement with (3); to this aim, the actual value of the toughness parameter G_c in (1) must be chosen to yield σ_c as limit stress, see for instance [12]. In particular, the damage field localizes in the central cross-section and a crack stems from the upper or lower surface depending on the sign of the applied bending moment. Since the stress fields are uniform along the beam axis to obtain robustly a localization in the center a very small mesh imperfection is placed in the central cross-section where the actual thickness equals $0.999\,h$. We associated a color to each point by computing, one step after reaching the limit, the crack depth d, and by comparing it to the beam thickness. For $\bar{N} \ge 0$ we observe snap-back solutions where the whole central cross-sections are suddenly cracked: $d/h \simeq 1$ and the points are reported in blue. Instead for compressive axial loads $\bar{N} < 0$ we observe partial fractures of the central cross-section where $d/h < 1$; according to the color-scale included in Fig. 2, the more intense is the compression the less deep is the crack.

Our objective is to include the information described above into a genuinely one-dimensional beam model, say *e.g.* Euler–Bernoulli, in order to obtain a one-dimensional damaging beam model. This is a problem of dimensional reduction where the main difficulty lies in determining suitable Ansatz in the thickness variable for the displacement, stress and damage fields.

A naïve attempt in this direction is to split the elastic energy density into stretching and bending contributions, as done in most beam or shell theories, while maintaining a single scalar damage field to modulate as a whole the elastic energy, see for instance [6,13–18]. For instance, in [15], the functional (1) is adapted as follows:

$$\mathcal{E}_S = \int_A \Big(m(\alpha)\Psi_e^+(\mathbf{E}_m, \mathbf{K}) + \Psi_e^-(\mathbf{E}_m, \mathbf{K}) \Big)\mathrm{d}A + G_c \int_A \left(\frac{(1-\alpha)^2}{4\delta} + \delta|\nabla\alpha|^2 \right)\mathrm{d}A. \tag{4}$$

In this formulation, A represents the mid-surface of the shell, Ψ_e is the elastic energy per unit surface, dependent on the membrane deformation $\mathbf{E}_m$ and the curvature $\mathbf{K}$ of A. The superscripts $\pm$ in Ψ_e account for the assumption that the total strain is decomposed into tensile and compressive contributions, enabling the modeling of material cracking in tension but not in compression. However, as already shown in [19,20], these choices have several drawbacks as they necessarily lead to an elliptical elastic domain in the

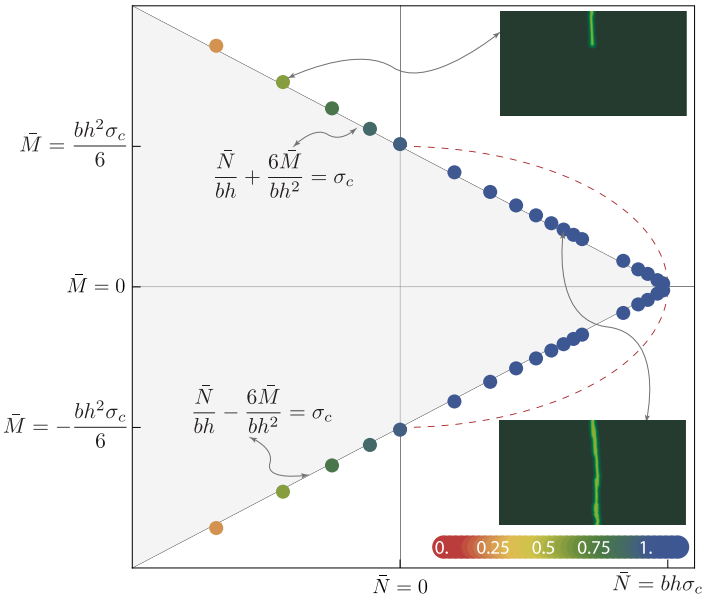

Fig. 2. Elastic domain as in (3) and evidence of numerical simulations within the plane (N, M) of stress characteristics. The points are the computed limits of the elastic domain and their colors correspond to the ratio d/h between the crack depth and the thickness a step after reaching the elastic boundary (see the two insets). (For interpretation of the references to color in this figure legend, the reader is referred to the web version of this article.)

(N, M) plane (see the dashed red curve in Fig. 2) and they cannot account for coupling between stretching and bending emerging when the damage breaks the mid-plane symmetry.

The model proposed in [21] goes a step further by postulating for the damage field $\alpha(x, y)$ a double sigmoid distribution in the thickness direction tuned by two different damage descriptors $y_U(x)$ and $y_L(x)$. However, they consider only bending deformations for the beam which is supposed inextensible; this assumption makes not possible the comparison with the full two-dimensional case described above.

1.2. Plan of the paper

Here we propose a damaging beam model with the following features:

1. similarly to [21], two phase-field damage parameters are adopted to describe the material fracturing; however our fracture interface is not diffuse but sharp;
2. the stress field S_{xx} is affine in the thickness coordinate y and depends linearly on the axial force N and the bending moment M.

Our model is detailed in Section 2. In Section 3, we prove that our choice leads to an excellent agreement with the 2D evidences described above in term of elastic domain and localization properties. Finally Section 4 describes a coupled problem on a statically undetermined beam where stretching and bending interplay significantly to obtain the correct solution. Conclusions and perspectives are drawn in Section 5. Lastly, Appendix furnishes additional details regarding the finite element simulations.

2. Formulation of the phase-field model for damaging beams

We first show that assuming a sharp-interface description for the damaged two-dimensional beam domain leads to estimate a smooth variation of the beam stiffnesses. Then we formulate the variational problem for a damaging Euler–Bernoulli beam.

2.1. Sharp-interface damaged domain

Specifically, let $\Omega^{(0,0)} = [0, L] \times [-b/2, b/2] \times [-h/2, h/2]$ be the pristine domain occupied by the beam-like body in its reference configuration. The damaged domain is described by the set

$$\Omega^{(\alpha,\beta)} := \left\{ 0 \le x \le L,\ y \in \mathbb{R},\ \frac{(\beta(x) - 1)\, h}{2} \le y \le \frac{(1 - \alpha(x))h}{2}, -b/2 \le z \le b/2 \right\}. \tag{5}$$

In order for $\Omega^{(\alpha,\beta)}$ to be a subset of $\Omega^{(0,0)}$, the two functions α and β must satisfy, for any $x \in [0, L]$, the conditions $\alpha(x) \ge 0$, $\beta(x) \ge 0$ and $\alpha(x) + \beta(x) \le 2$.

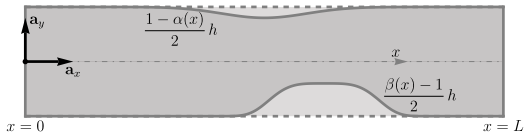

Fig. 3. Sharp interface description of the two-dimensional damaged domain.

The two non-negative scalar functions, α and β completely characterize the damaged domain and will be chosen as the phase-field damage variables. They respectively mean the "erosion" from above and from below of the pristine beam, see Fig. 3. When $\alpha(x) = \beta(x) = 0$, the cross-section in x maintains its original thickness h, whilst, at the opposite, when $\alpha(x) + \beta(x) = 2$ its thickness vanishes.

Other more complex choices are possible to capture the geometry of the damaged domain; for instance, one can grade the damage level on a scale from 0 to 1 or one can add another field to describe the erosion of the beam cross-section around its midline. However we limit the attention to the minimal choice allowing to describe independently fracture processes both symmetrical and non-symmetrical with respect to the beam mid-line. The choice made of considering damages stemming from the top or bottom surfaces seems the most appropriate from the physical point of view. As it will be clear in the following, the functions α and β must have square-integrable spatial derivatives, say $\alpha \in H^1(0, L)$ and $\beta \in H^1(0, L)$. Therefore, the top and bottom surfaces of the damaged domain can have isolated points where their normal jumps.

Moreover, it is natural to assume that damage is irreversible. This translate in the following requests for the phase-fields time derivatives

$$\frac{\partial}{\partial t}\alpha(x,t) \geq 0, \quad \frac{\partial}{\partial t}\beta(x,t) \geq 0, \tag{6}$$

for every point $x \in [0, L]$ and every instant t.

2.2. Stress distribution and elastic energy density

Closely following the exact solution of the Saint-Venant problem for the undamaged body $\Omega^{(0,0)}$ under axial force and bending, we postulate that the only non-vanishing stress component is the normal stress S_{xx}. This is assumed affine in the y coordinate, namely

$$\boldsymbol{S}(x,y) := S_{xx}(x,y)\,\boldsymbol{a}_x \otimes \boldsymbol{a}_x, \quad \text{with} \quad S_{xx}(x,y) = \sigma_0(x) + y\,\sigma_1(x). \tag{7}$$

The functions σ_0, σ_1 can be determined in terms of axial force and bending moment thanks to the geometry of the damaged body $\Omega^{(\alpha,\beta)}$ to satisfy

$$b\int_{-(1-\beta(x))h/2}^{(1-\alpha(x))h/2} \big(\sigma_0(x) + y\,\sigma_1(x)\big)\,\mathrm{d}y = N(x), \qquad b\int_{-(1-\beta(x))h/2}^{(1-\alpha(x))h/2} y\,\big(\sigma_0(x) + y\,\sigma_1(x)\big)\,\mathrm{d}y = M(x). \tag{8}$$

Defined the effective cross-section *area*

$$\mathsf{A}(\alpha,\beta) = b\int_{-(1-\beta)h/2}^{(1-\alpha)h/2} 1\,\mathrm{d}y = bh\,\frac{(2-\alpha-\beta)}{2}, \tag{9}$$

the effective cross-section *first moment of area*

$$\mathsf{S}(\alpha,\beta) = b\int_{-(1-\beta)h/2}^{(1-\alpha)h/2} y\,\mathrm{d}y = bh^2\,\frac{(\beta-\alpha)(2-\alpha-\beta)}{8}, \tag{10}$$

and the effective cross-section *moment of inertia*

$$\mathsf{J}(\alpha,\beta) = b\int_{-(1-\beta)h/2}^{(1-\alpha)h/2} y^2\,\mathrm{d}y = \frac{bh^3}{12}\,\frac{(2-\alpha-\beta)\left(1+\alpha^2+\beta^2-\alpha\beta-\alpha-\beta\right)}{2}, \tag{11}$$

Eqs. (8) are easily solved inverting a 2×2 linear system

$$\begin{pmatrix} \mathsf{A}(\alpha,\beta) & \mathsf{S}(\alpha,\beta) \\ \mathsf{S}(\alpha,\beta) & \mathsf{J}(\alpha,\beta) \end{pmatrix} \begin{pmatrix} \sigma_0 \\ \sigma_1 \end{pmatrix} = \begin{pmatrix} N \\ M \end{pmatrix}. \tag{12}$$

Note that the elastic energy density, say $\mathcal{E}$, for the damaged body is readily determined in terms of the stress descriptors. Indeed,

$$\mathcal{E} = \frac{1}{2}\int_{\Omega^{(\alpha,\beta)}} \mathbb{F}\boldsymbol{S} \cdot \boldsymbol{S}\,\mathrm{d}x\mathrm{d}y = \frac{1}{2}\int_{\Omega^{(\alpha,\beta)}} \frac{S_{xx}^2}{\mathsf{E}}\,\mathrm{d}x\mathrm{d}y, \tag{13}$$

where the material has been supposed isotropic $\mathbb{F}\boldsymbol{S} = [(1+\nu)\boldsymbol{S} - \nu\,\mathrm{tr}\boldsymbol{S}\,\mathbf{1}]/\mathsf{E}$, E is the Young modulus, ν the Poisson ratio, tr is the trace operator and $\mathbf{1}$ is the identity tensor in $\mathbb{R}^2$. Its trivial to verify that

$$\mathcal{E} = \frac{1}{2}\int_0^L \left[\frac{1}{\mathsf{E}}\begin{pmatrix} \mathsf{A}(\alpha,\beta) & \mathsf{S}(\alpha,\beta) \\ \mathsf{S}(\alpha,\beta) & \mathsf{J}(\alpha,\beta) \end{pmatrix}^{-1} \begin{pmatrix} N \\ M \end{pmatrix} \cdot \begin{pmatrix} N \\ M \end{pmatrix}\right] \mathrm{d}x. \tag{14}$$

This means that the elastic energy of the damaged body is completely characterized as a function of A, S and J the effective geometric properties of the cross-sections.

2.3. Beam constitutive relations

Once postulated the stress distribution (7), the constitutive relations are derived via the following maximization problem

$$\max_{\boldsymbol{S}} \int_{\Omega(\alpha,\beta)} \left(\boldsymbol{S} \cdot \boldsymbol{E}(\boldsymbol{u}) - \frac{\mathbb{F}\boldsymbol{S} \cdot \boldsymbol{S}}{2} \right), \tag{15}$$

where $\boldsymbol{E}(\boldsymbol{u})$ is a suitable choice of the strain field in terms of displacement $\boldsymbol{u}$.

Specifically, to obtain the simple Euler–Bernoulli beam we assume

$$\boldsymbol{u}(x,y) := \big(w(x) - y\, v'(x)\big)\ \boldsymbol{a}_x + v(x)\, \boldsymbol{a}_y \tag{16}$$

where w and v are respectively the axial and transverse displacement fields averaged through the thickness. Using (16) the strain has only one non-vanishing component, namely

$$\boldsymbol{E}(\boldsymbol{u}) = E_{xx}\, \boldsymbol{a}_x \otimes \boldsymbol{a}_x, \text{ with } E_{xx} = w'(x) - y\, v''(x) =: \varepsilon(x) + y\, \chi(x), \tag{17}$$

with E_{xx} an affine function of y representing the elongation of the beam fibers. Notice that with the terms "Euler–Bernoulli beam" we intend a beam which at the same time is able to bend and stretch. Solving (15) we get the EB constitutive relation

$$\begin{pmatrix} N \\ M \end{pmatrix} = \begin{pmatrix} \mathsf{EA}(\alpha,\beta) & \mathsf{ES}(\alpha,\beta) \\ \mathsf{ES}(\alpha,\beta) & \mathsf{EJ}(\alpha,\beta) \end{pmatrix} \begin{pmatrix} \varepsilon \\ \chi \end{pmatrix}, \tag{18}$$

in terms of the average elongation $\varepsilon = w'$ and the curvature $\chi = -v''$. Therefore, EA is the axial stiffness of the damaged beam, EJ is the bending stiffness whilst the term ES controls the coupling between stretching and bending that emerges in every cross-section x where $\alpha(x) \neq \beta(x)$. If the beam is homogeneous and in its original state, there is no coupling. However, the moment a crack initiates from either the top or bottom, the constitutive relation becomes inherently coupled. Note that the stiffness ES contains information on the actual placing of the center of area in the eroded cross-sections; it is therefore responsible for the distortion of the beam neutral axis due to damage.

The dependence of all these stiffnesses on the damage descriptor, α and β, is presented in Fig. 4*a*, *b*, *c*. Fig. 4*d* compares these stiffnesses (solid lines) with the results analytically determined using the asymptotic sharp interface model presented in [19] (dotted lines) assuming a damage that develops exclusively on the upper side of a beam until complete fracture, *i.e.* $\alpha \in [0,2], \beta = 0$. The impact of a crack, originating from the upper boundary and extending to a depth of $h\alpha$, manifests itself in a distinct manner on the stiffness properties. As one would expect, the axial stiffness monotonically diminishes with the growth of the crack. Contrastingly, the bending stiffness experiences a swift decline upon the initiation of the crack, followed by a plateau as the crack extends to the beam's centerline. Indeed, a significant reduction in moment of inertia occurs when material is absent from the top and bottom of the beam, but removal of material from the central part has a comparatively negligible impact on the inertia.

Remark 1. We have used the simplest possible Ansatz for both the stress and the strain fields. However, one could have chosen the same kinematics of an Euler–Bernoulli beam but a richer stress distribution. For instance, one could add suitable descriptions for the other stress components, say S_{xy} or S_{yy}, which emerge once the beam cross-sections are damaged. For instance, to satisfy the traction-free condition on the damaged top surface $\boldsymbol{S}\boldsymbol{n} = \boldsymbol{0}$ would call for shear stresses depending on the phase-field derivative α', see Fig. 5. These additional terms would enter in the elastic energy and produce a different beam theory. Similar more refined theories are not discussed here and will be the subject of future investigations.

2.4. Variational formulation of a damaging EB beam

This section is devoted to formulate the discrete-time evolution for the damaging Euler–Bernoulli beam as a set of sequential minimization problems. More specifically we discretize the relevant time interval $[0,T]$ considering only the time instants $t_i \in [t_0 = 0, t_1, t_2, \dots, t_I = T]$. We assume that $\alpha_0 = 0$ and $\beta_0 = 0$ at $i = 0$.

Having deduced the form of the elastic energy from (14), (18),

$$\mathcal{E}(w,v,\alpha,\beta) = \frac{1}{2} \int_0^L \left(\mathsf{EA}(\alpha,\beta)(w')^2 + 2\,\mathsf{ES}(\alpha,\beta) w' v'' + \mathsf{EJ}(\alpha,\beta)(v'')^2 \right) \mathrm{d}x, \tag{19}$$

and assigned a linear functional for the external work of the axial q_{t_i} and transversal p_{t_i} loads at time t_i

$$\mathcal{W}_i(w,v) = \int_0^L \left(q_{t_i}\, w + p_{t_i}\, v \right) \mathrm{d}x, \tag{20}$$

it remains to establish how the energy is dissipated in the damaging processes. To this aim we assume a rate-independent material, see [22,23], and postulate for the dissipation

$$\mathcal{D}_i(\alpha,\beta) = \int_0^L \mathsf{w}_c \left(\hat{\mathsf{c}}_i\, \alpha + \check{\mathsf{c}}_i\, \beta + \frac{\ell^2}{2} (\alpha'^2 + \beta'^2) \right) \mathrm{d}x. \tag{21}$$

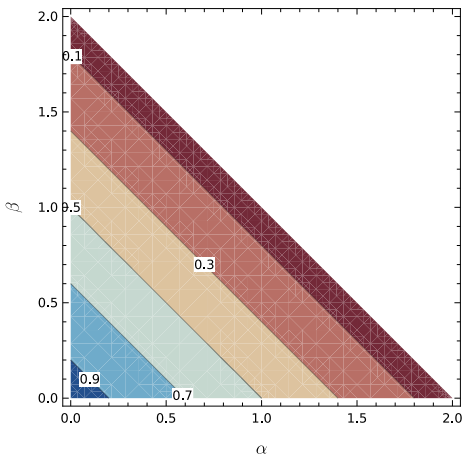

(a) Contour plot of $\mathsf{EA}(\alpha,\beta)/\mathsf{EA}(0,0)$.

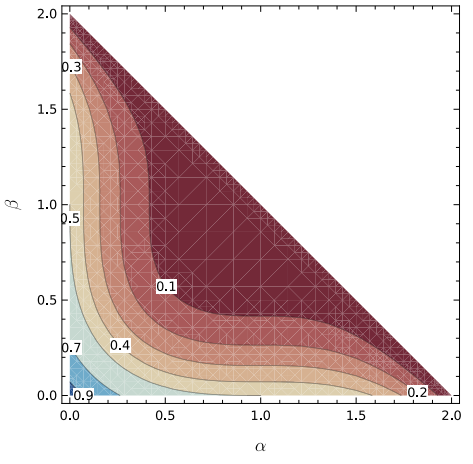

(b) Contour plot of $\mathsf{EJ}(\alpha,\beta)/\mathsf{EJ}(0,0)$.

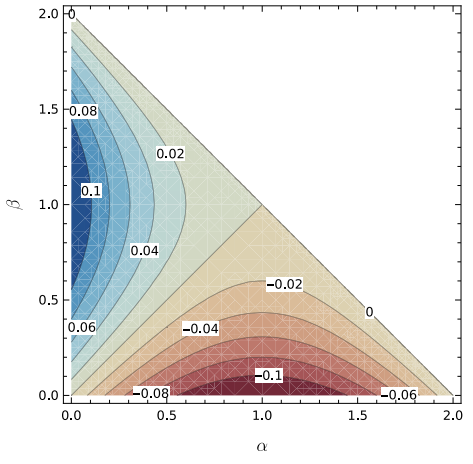

(c) Contour plot of $\mathsf{S}(\alpha,\beta)$.

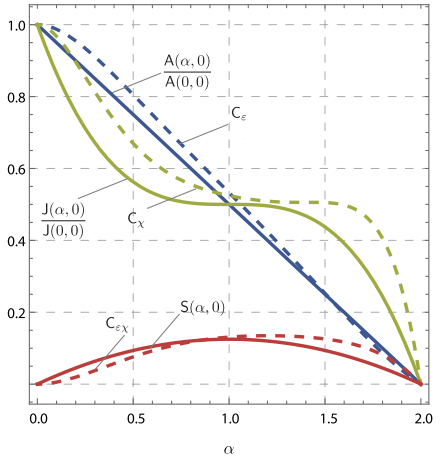

(d) Normalized stiffnesses for $\beta = 0$.

Fig. 4. Stiffnesses in (18) as functions of the damage parameters α and β. In (d) normalized stiffnesses for $\beta = 0$ (solid line), compared with those determined in [19] (dotted line): A corresponds to C_ε, J to C_χ, and S to $\mathsf{C}_{\varepsilon\chi}$.

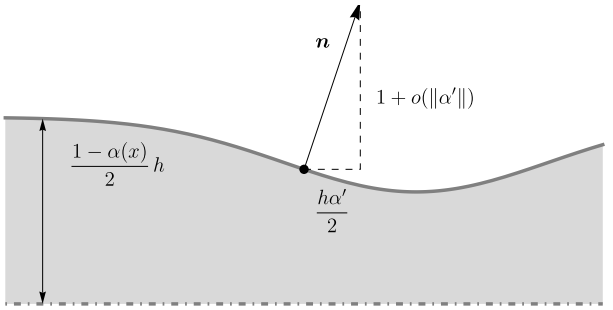

Fig. 5. First order approximation of the normal to the top damaged surface.

The step-dependent parameters $\hat{\mathsf{c}}_i$ and $\check{\mathsf{c}}_i$ measure the energy per unit area dissipated in the erosion of half cross section. We assume

$$\hat{\mathsf{c}}_i = \begin{cases} 1 & \text{if } \hat{\sigma}_{i-1} \geq 0 \\ \mathsf{c}_\infty & \text{if } \hat{\sigma}_{i-1} < 0 \end{cases}, \qquad \check{\mathsf{c}}_i = \begin{cases} 1 & \text{if } \check{\sigma}_{i-1} \geq 0 \\ \mathsf{c}_\infty & \text{if } \check{\sigma}_{i-1} < 0 \end{cases}, \tag{22}$$

with $\mathsf{c}_\infty \gg 1$. Here $\hat{\sigma}_{i-1}$ and $\check{\sigma}_{i-1}$ are respectively the values at step $i-1$ of the stress at the upper and bottom surfaces, respectively. By using (12) and (18), these last can be readily computed as functions of the elongation and curvature in the same cross-section. Finally $\ell \ll L$ is a characteristic length controlling the width of the damage localization zones. With the previous choices, the creation of damages under compression are related to large energy losses $\mathsf{c}_\infty \gg 1$ and are, therefore, avoided; numerically we obtain the same results as in the usual energy splitting methods, see *e.g.* [4]. Therein damage evolution under compression is avoided postulating that the elastic energy does not depend on damage for the compressive strain components. For a beam where the damage phase-fields are sufficiently smooth, this choice does not seem physically acceptable, see *e.g.* Fig. 3. Indeed, the axial and bending stiffnesses are actually reduced independently of the signs of the axial force and bending moments.

A discrete-time evolution for the damaging Euler–Bernoulli beam corresponds to the sequential minimizations

$$\min_{(\alpha,\beta)\in K_i, w\in H^1, v\in H^2} \mathcal{F}_i(w,v,\alpha,\beta) := \mathcal{E}(w,v,\alpha,\beta) + \mathcal{D}_i(\alpha,\beta) + \mathcal{W}_i(w,v), \tag{23}$$

where damage parameters at time t_i are constrained to belong to the functional space

$$K_i = \left\{(\alpha,\,\beta) \in H^1 \times H^1, \alpha \geq \alpha_{i-1} \geq 0,\ \beta \geq \beta_{i-1} \geq 0,\ \alpha+\beta \leq 2\right\}, \tag{24}$$

in order to satisfy the irreversibility condition and produce a finite value for the dissipation.

Remark 2. It is crucial to emphasize that our damage model is subject to regularization on the beam axis, meaning that the damage fields α and β solely rely on the $x-$coordinate. Within the cross-section, it can be regarded as a simplified sharp-interface model, indicating that the material is either undamaged or completely fractured. This arises from our application of a structural theory, which typically leads to a substantial loss or reduction of information concerning the fields within the cross-section.

3. Elastic domain and localization properties

3.1. Elastic domain

The elastic domain associated to the functionals $\mathcal{F}_i$ is found requiring that the elastic solution, characterized by $\alpha(x) = \beta(x) = 0$, is stable (*i.e.* a proper minimum).

For the elastic branch to be stable it suffices to require the non negativity of the Frechet derivatives along the directions α and β evaluated $\alpha(x) = \beta(x) = 0$:

$$\begin{cases} \displaystyle\int_0^L \left(\mathsf{EA}_{,\alpha}\frac{w'^2}{2} + \mathsf{ES}_{,\alpha}w'v'' + \mathsf{EJ}_{,\alpha}\frac{v''^2}{2} + \mathsf{w}_c\hat{\mathsf{c}}_i\right)_{\alpha=\beta=0} \mathrm{d}x \geq 0, \\ \displaystyle\int_0^L \left(\mathsf{EA}_{,\beta}\frac{w'^2}{2} + \mathsf{ES}_{,\beta}w'v'' + \mathsf{EJ}_{,\beta}\frac{v''^2}{2} + \mathsf{w}_c\check{\mathsf{c}}_i\right)_{\alpha=\beta=0} \mathrm{d}x \geq 0. \end{cases} \tag{25}$$

Indeed, all the admissible variations $\tilde{\alpha}$ and $\tilde{\beta}$ must be non-negative if stemming from the undamaged state. With straightforward but cumbersome calculations, the previous conditions are expressed in terms of axial force and bending moment as

$$\begin{cases} \displaystyle\int_0^L \left(-\frac{(6M+hN)^2}{4bh^3\mathsf{E}} + \mathsf{w}_c\hat{\mathsf{c}}_i\right) \mathrm{d}x \geq 0, \\ \displaystyle\int_0^L \left(-\frac{(6M-hN)^2}{4bh^3\mathsf{E}} + \mathsf{w}_c\check{\mathsf{c}}_i\right) \mathrm{d}x \geq 0. \end{cases} \tag{26}$$

Using standard localization arguments on (26), the elastic domain in the cross-section x is given by

$$\begin{cases} (6M+hN)^2 = 4bh^3\mathsf{E}\mathsf{w}_c & \text{for } 6M+hN > 0, \\ (6M+hN)^2 = 4bh^3\mathsf{E}\mathsf{w}_c\mathsf{c}_\infty & \text{for } 6M+hN \leq 0, \\ (6M-hN)^2 = 4bh^3\mathsf{E}\mathsf{w}_c & \text{for } 6M-hN > 0, \\ (6M-hN)^2 = 4bh^3\mathsf{E}\mathsf{w}_c\mathsf{c}_\infty & \text{for } 6M-hN \leq 0, \end{cases} \tag{27}$$

which perfectly agree with (3) once chosen $\mathsf{w}_c = bh\sigma_c^2/(4\mathsf{E})$ and $\mathsf{c}_\infty \to +\infty$.

Hence, the elastic domain in the plane (N, M) for the proposed EB damaging beam (23) is the unbounded triangular region with vertex in $(N = N_c = bh\sigma_c, M = 0)$ and sides passing through the points $(N = 0, M = \pm M_c = \pm bh^2\sigma_c/6)$, see Fig. 2 or Fig. 6.

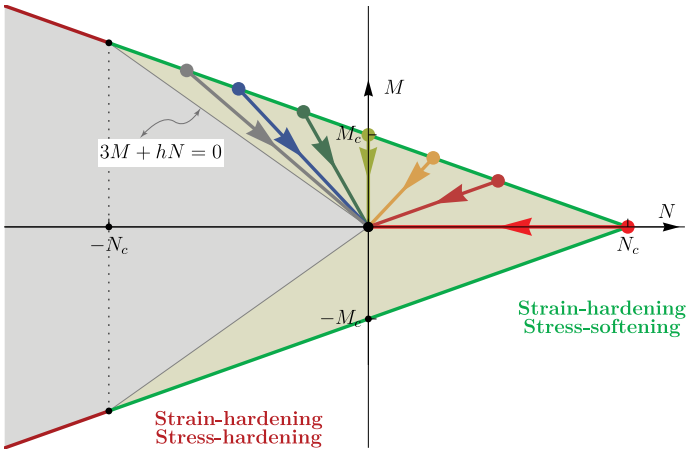

Fig. 6. Strain and stress hardening character on the boundary of the elastic domain. The arrows pointing to the origin represent the paths used in Section 3.3 to deduce the model localization properties. (For interpretation of the references to color in this figure legend, the reader is referred to the web version of this article.)

3.2. Strain-hardening and stress-softening of the damaging law

The strain and stress hardening character of the constitutive law (18) are computed considering the behavior of the elastic domains in term of strains and in term of stresses under admissible variations of the damage parameters from $\alpha = \beta = 0$.

In particular, we start considering $M > 0$; since for positive bending moments the maximal stress is on the top surface, the only damage parameter that can evolve is α. Considering the elastic domain in terms of strains

$$\mathcal{Y}(\alpha) = \left\{ -\frac{\partial}{\partial \alpha} \begin{pmatrix} \mathsf{A}(\alpha,0) & \mathsf{S}(\alpha,0) \\ \mathsf{S}(\alpha,0) & \mathsf{J}(\alpha,0) \end{pmatrix} \begin{pmatrix} \varepsilon \\ \chi \end{pmatrix} \cdot \begin{pmatrix} \varepsilon \\ \chi \end{pmatrix} \leq 2\mathsf{w}_c/\mathsf{E} \right\}, \tag{28}$$

and computing its derivative with respect to α evaluated in $\alpha = 0$, we can easily deduce that this set grows when $\chi(2\varepsilon + h\chi) > 0$ or in terms of stresses when $M(6M + h\,N) > 0$. Similarly, for negative bending moments, the same reasoning in terms of β leads to the condition $M(h\,N - 6M) < 0$. The growth of the elastic domain, as damage evolves, correspond to a strain-hardening response. From the results above, it is immediate to see that on the whole boundary of the elastic domain (27) the response has a *strain-hardening* character in both the strain measures.

The elastic domain in term of stresses, for $M > 0$, is given by

$$\mathcal{Y}^*(\alpha) = \left\{ \frac{\partial}{\partial \alpha} \left[\begin{pmatrix} \mathsf{A}(\alpha,0) & \mathsf{S}(\alpha,0) \\ \mathsf{S}(\alpha,0) & \mathsf{J}(\alpha,0) \end{pmatrix}^{-1} \right] \begin{pmatrix} N \\ M \end{pmatrix} \cdot \begin{pmatrix} N \\ M \end{pmatrix} \leq 2\mathsf{E}\mathsf{w}_c \right\}. \tag{29}$$

After computing the derivative of $\mathcal{Y}^*(\alpha)$ with respect to α evaluated in $\alpha = 0$, we deduce that this set shrinks (*i.e.* stress-softening) when $(3M + hN)(6M + hN) > 0$. Since the condition $3M + hN = 0$ intersects the boundary $6M + hN = hN_c$ at $N = -N_c$, not the whole boundary of the elastic domain (27) has a *stress-softening* character but only its points where $N \geq -N_c$. The stress-hardening tendency for large compression is confirmed by conducting a second analysis involving negative bending moments and variations with respect to β.

We summarize these features in the diagram of Fig. 6, highlighting in green the stress-softening boundary and in red the stress-hardening boundary. We shall proceed to numerically evaluate the points along the boundary of the elastic domain, with the results depicted in Fig. 12.

3.3. Localization properties

Under monotonically increasing loads, when the boundary of the elastic domain is reached, the undamaged elastic solution looses its stability and any subsequent equilibrium branch is characterized by the evolution of the damage parameters. We show, under certain conditions, the phase-fields α and β localize in narrow strips whose width is controlled by the characteristic length ℓ.

To this aim, we simplify the applied loads considering the case examined in Section 1: axial forces $\bar{N}_i$ and bending moments $\bar{M}_i$ are applied at the beam end points and are increased with each step i. For a sufficient number of steps, there is a subinterval $\mathcal{D} \subseteq [0, L]$ where limit stresses are reached, say $(\bar{N}_*, \bar{M}_*) \in \mathcal{Y}^*$, and consequently damage can evolve. In particular, we show that if $(\bar{N}_*, \bar{M}_*)$ belong to the stress-softening part of the boundary of the elastic domain, *i.e.* $\bar{N}_* \geq -N_c$, the evolution of damage is concentrated in a narrow interval having length proportional to ℓ.

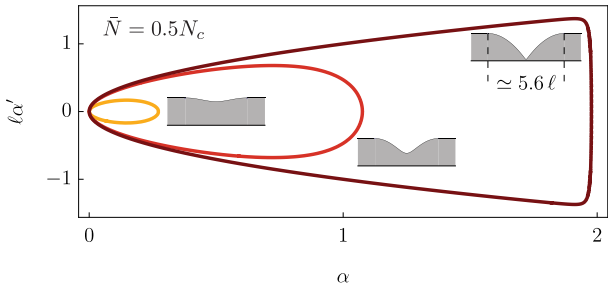

Fig. 7. The phase portrait of the differential equations representing the development of damage field.

To this aim, we exploit the fact that the functionals $\mathcal{F}_i$ are independent on x and, therefore, possess a first integral; one can check that the quantity

$$I(x) = \left(\frac{1}{1-\frac{\mathsf{S}^2(\alpha,\beta)}{\mathsf{A}(\alpha,\beta)\mathsf{J}(\alpha,\beta)}}\right)\left(\frac{\mathsf{S}(\alpha,\beta)\,\bar{N}\bar{M}}{\mathsf{EA}(\alpha,\beta)\mathsf{J}(\alpha,\beta)} - \frac{\bar{N}^2}{2\mathsf{EA}(\alpha,\beta)} - \frac{\bar{M}^2}{2\mathsf{EJ}(\alpha,\beta)}\right) + \mathsf{w}_c\left(\hat{\mathsf{c}}_i\,\alpha + \check{\mathsf{c}}_i\,\beta + \frac{\ell^2}{2}\,(\alpha'^2+\beta'^2)\right) \tag{30}$$

is actually a constant: $\partial I(x)/\partial x = 0$. Evaluating the constant in a region where the damage is zero gives a differential equation for the damage profiles. Clearly, due to the softening character of the response, the damage profiles exist and evolve only for a sequence of applied loads $(\bar{N}_i, \bar{M}_i)$ starting from $(\bar{N}_*, \bar{M}_*)$ and tending to $(0,0)$ (complete fracture). For these sequences we choose the linear paths shown in Fig. 6 by color arrows. For more details on the construction of the damage profile, the interested reader is referred to [24].

3.4. Non-symmetric cracks: $\bar{M}_* > 0$, $\bar{N}_* \gtrless 0$

Without loss of generality we can assume a positive bending moment $\bar{M}_* > 0$; therefore, as $\hat{\sigma}_i > \check{\sigma}_i$ at any step i the crack could stem only from the top surface and $\beta = 0$. Negative moments are treated similarly but induce the evolution of β with $\alpha = 0$.

From (30), the differential equation for the damage profile is

$$(\ell\,\alpha')^2 = \frac{\alpha\left(3\alpha^3 + 2\alpha^2\left(m^2+3n^2-9\right) + 12\alpha\left(3-m^2+n^2\right) + 24(m+n-1)(m+n+1)\right)}{3(\alpha-2)^3}, \tag{31}$$

depending on both $n := N/N_c$ and $m := M/M_c$.

For $(\bar{N},\bar{M}) = (\bar{N}_*,\bar{M}_*) \in \mathcal{Y}^*$ we have $m = 1-n$ and the rhs of (31) has only one non-negative root $\alpha = 0$. Therefore the maximum value in the damage profile vanishes.

However, due to the softening character of the response, we assume a linear path from the point $(\bar{N}_*,\bar{M}_*)$ to the origin of the stress space, namely $(n,m) = \tau\,(\bar{N}_*/N_c, \bar{M}_*/M_c)$ with τ decreasing from 1 to 0, cfr. the color paths of Fig. 6. Then, for $1 > \tau \geq 0$, the rhs of (31) is a function of α with two non-negative roots, $\alpha = 0$ and $\alpha = \alpha_{\max}(\tau) < 2$, and one maximum between them, $0 < \alpha_{\text{flex}}(\tau) < \alpha(\tau)$. In such a case the integration of the actual damage profile $\alpha_\tau(x)$ can be easily done: these roots correspond to the minimum and maximum values of the profile (where $\alpha'_\tau(x) = 0$), while the maximum correspond to a flex in the damage profile (where $\alpha''_\tau(x) = 0$).

Fig. 7 reports the curves (α,α') corresponding to (31) for the three monotonically decreasing values $\tau = 0.8, 0.5, 0.01$; associated to each curve we show the damage profile in the beam section. Note that these curves in Fig. 7 are nested without intersections. This means that in the construction of these successive damage profiles the irreversibility condition is necessarily satisfied and does not play an active role. Fig. 7 reports the curves (α,α') obtained for $\bar{N} = 0.5\,N_c$ (dark red path in Fig. 6), but similar curves (nested without intersections) can be obtained for all the other cases $-N_c \leq \bar{N} \leq N_c$.

Fig. 8*a* and *b* report respectively the decreasing values of the bending moments and the axial forces as the damage develops *i.e.* as functions of $\alpha_{\max}$. Note the different character of the bending moment curves in presence of compression (say *e.g.* blue curve) and in presence of traction (say for instance dark red curve).

Clearly when $\alpha_{\max} \to 2$ the damage has completely eroded the beam thickness and, for all the cases, we have $N \to 0$ and $M \to 0$. This limit damage profile represents the phase-field approximation of the fully developed crack and can be computed analytically from (31) with $n \to 0$ and $m \to 0$. When centered in $x = \bar{x}$, it reads

$$\alpha_{(\tau=0)}(x) = \begin{cases} 2 - \sqrt{2}(x-\bar{x})/\ell + (x-\bar{x})^2/(4\ell^2), & \bar{x} \leq x \leq \bar{x} + 2\sqrt{2}\ell, \\ 2 - \sqrt{2}(x-\bar{x})/\ell + (x-\bar{x})^2/(4\ell^2), & \bar{x} - 2\sqrt{2}\ell \leq x \leq \bar{x}. \end{cases} \tag{32}$$

Its support equals $4\sqrt{2}\,\ell \simeq 5.6\,\ell$, whilst the energy dissipated in its creation is $4\sqrt{2}\,\mathsf{w}_c\ell$, see (21). Remark that this localized limit profile is independent of the compression or traction value provided $-N_c < N < N_c$.

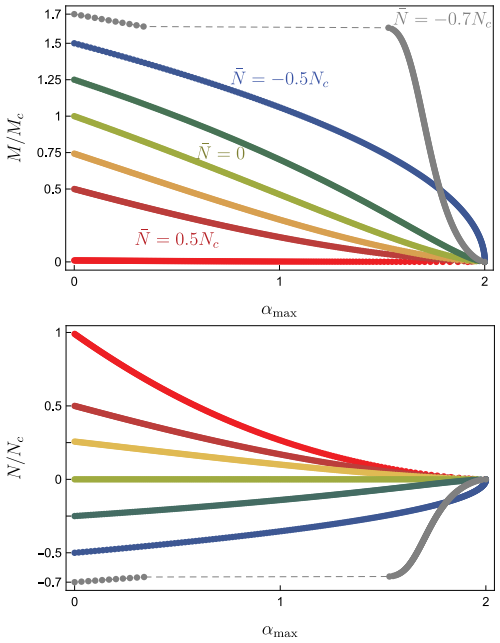

Fig. 8. Softening responses in terms of bending moments (top) and axial forces (bottom). The red curves correspond to the symmetric crack: for this case on the abscissæ of both plots one should read $(\alpha_{\max} + \beta_{\max})$ instead of $\alpha_{\max}$. (For interpretation of the references to color in this figure legend, the reader is referred to the web version of this article.)

3.5. Symmetric case: $\bar{M}_* = 0$

Only for reference with the standard traction test on a bar, we consider the case with vanishing bending moment $\bar{M}_* = 0$. The beam maintains its mid-line symmetry and we can assume $\hat{c}_i = \check{c}_i = 1$, and $\alpha = \beta$. Eq. (30) reduces to

$$-\frac{\bar{N}_*^2}{2\mathsf{EA}(0,0)} = -\frac{\bar{N}_*^2}{2\mathsf{EA}(\alpha,\alpha)} + 2\mathsf{w}_c\,\alpha - \ell^2\,\mathsf{w}_c\alpha'^2, \tag{33}$$

the constant on the lhs being evaluated in a point where $\alpha = 0$ and $\alpha' = 0$. Expressing w_c in terms of the critical value N_c, we are left to integrate the differential equation

$$(\ell\alpha')^2 = 2n^2\left(1 - \frac{\mathsf{A}(0,0)}{\mathsf{A}(\alpha,\alpha)}\right) + 2\alpha = 2\alpha\left(1 - \frac{n^2}{1-\alpha}\right), \tag{34}$$

with $n = N/N_c$ decreasing from 1 to 0. The curves (α, α') corresponding to (34) are nested without intersections as in the previous case. Again the maximal value of α is found as the positive non-vanishing root of the rhs of (34), namely

$$\alpha_{\max}(n) = \beta_{\max}(n) = 1 - n^2. \tag{35}$$

This maximal damage value increases as the stress n is decreased (softening response). These properties guarantees that in the integration of two successive damage profiles the irreversibility conditions does not play a role. The limit damage profile is achieved for $n \to 0$; it is now symmetric with respect to the beam axis and, when centered in $x = \bar{x}$, it reads

$$\alpha_0(x) = \beta_0(x) = \begin{cases} 1 - \sqrt{2}(x-\bar{x})/\ell + (x-\bar{x})^2/(2\ell^2), & \bar{x} \le x \le \bar{x} + \sqrt{2}\ell, \\ 1 - \sqrt{2}(x-\bar{x})/\ell + (x-\bar{x})^2/(2\ell^2), & \bar{x} - \sqrt{2}\ell \le x \le \bar{x}. \end{cases} \tag{36}$$

Its support equals $2\sqrt{2}\,\ell$ (twice smaller than the generic case above), whilst the energy dissipated in its creation is $8\sqrt{2}\,\mathsf{w}_c\ell/3$ (0.67 times smaller than the generic case above). All these results coincide, modulo a change of variables, with the well known properties derived in the literature, see *e.g.* [24], for a bar under tension.

However, it is clear that assuming $\bar{M}_* = 0$ and a perfectly symmetric evolution with $\alpha(x) = \beta(x)$ is a pure idealization: any small imperfection in the beam axis, in the material or in the application of the load leads to the development of non-symmetric cracks as the one described in Section 3.4.

4. A simple numerical example

To demonstrate the predictive capacity of our model, we examine the evolution of a beam governed by (23) under a monotonically increasing transverse load $\lambda \ge 0$ applied to its midpoint (see Fig. 9). The beam is straight in its initial configuration

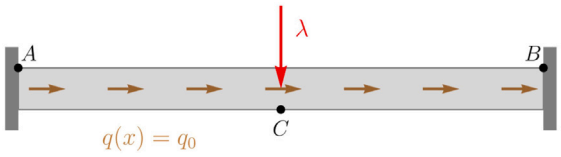

Fig. 9. Setup of the numerical experiment. The contemporary presence of a transverse and an axial load induces a different evolution of the damage variables in the points A and B: the cross section of A is indeed under traction whilst the cross section of B is compressed.

and also subject to a constant distributed axial load $q(x) = \bar{q}$ for $x \in [0, L]$; the presence of such a load allow us to enlighten the difference with the existing literature models. We have chosen $\bar{q} = 1.4\, bh\sigma_c/L > 0$; this value is large enough to produce a non negligible effect but small enough to do not produce any damage without the aid of the transverse force.

Despite the simplicity of the proposed set-up, any model not accounting for the coupling between axial and bending deformations fails to capture the correct response.

The evolution of the relevant fields $N(x)$, $M(x)$, $\alpha(x)$ and $\beta(x)$, as the transverse load is monotonically increased, are described analytically below for what is feasible. They have been also computed via a Finite Element code discretizing the functional (23); the details are outlined in Appendix. The analytical and numerical results are in perfect agreement.

We first compute the elastic response assuming a vanishing initial damage for $\lambda = 0$. Due to the model rate-independence and to the monotonically increasing character of the transverse load, λ can be confused with time. Hence, for sufficiently small $\lambda > 0$, the response is elastic and described by the fields

$$N_0(x) = \bar{q}\left(\frac{L}{2} - x\right), \quad M_0(x) = \frac{\lambda L}{8}\mathfrak{h}(x), \quad \alpha(x) = \beta(x) = 0, \tag{37}$$

where $\mathfrak{h}(x)$ is the piecewise function linearly interpolating between the three values $\mathfrak{h}(0) = 1$, $\mathfrak{h}(L/2) = -1$ and $\mathfrak{h}(L) = 1$. The fields N_0 and M_0 are plotted in Fig. 11 as solid black lines. Standard linear beam theory is sufficient here to deduce the axial stress and the bending moment; note, however, that to compute N_0 and M_0 one has to solve the static indeterminacies. From the fields in (37), we can clearly deduce not only the axial strain $\varepsilon(x)$ and the curvature field $\chi(x)$ via (18), but also the stress field on the whole beam domain

$$\sigma_0(x, y) = \frac{N_0(x)}{bh} + 12y\frac{M_0(x)}{bh^3}; \tag{38}$$

this stress distribution is depicted in Fig. 10*a* through a suitable color scale. The response (37) is stable until the stress (38) is everywhere below the stress critical value σ_c. The highest positive tension is clearly in the point A of coordinates $(x = 0, y = h/2)$ where the positive contributions of the axial force $\bar{N}_0 := N_0(0) = \bar{q}L/2$ and of the bending moment $M_0(0) = \lambda L/8$ add up to determine $\sigma_A = \max_{x,y}\sigma_0(x, y)$. Equating this maximal value to σ_c and solving for λ allows to determine the first critical value for the transverse force[1]

$$\sigma_A = \frac{L}{2bh}\left(\bar{q} + \frac{3\lambda}{2h}\right) = \sigma_c \quad \Rightarrow \quad \lambda_{c1} = \frac{4bh^2\sigma_c}{3L} - \frac{2h\bar{q}}{3} \simeq 0.4\,\frac{bh^2\sigma_c}{L}. \tag{39}$$

Hence, the elastic response is stable for $\lambda \in [0, \lambda_{c1})$. When $\lambda > \lambda_{c1}$ this equilibrium branch looses its stability. In particular, due to the simultaneous presence of axial positive tension and bending moment the evolution of damage in the cross-section $x = 0$ for $\lambda > \lambda_{c1}$ is abrupt, cfr. Fig. 2; in other words numerical minimization of (23) leads directly from the stable elastic branch with $\alpha = 0$ to a stable branch where $\alpha = 2$ for $0 \le x \lesssim 2.5\,\ell$; due to a snap-back of the overall response we cannot observe any intermediate stable configuration where $0 < \alpha < 2$ near $x = 0$. The abrupt fracture has the effect of suddenly converting the statically underdetermined beam into a statically determined cantilever. Then, as soon as the transverse load exceeds λ_{c1} the equilibrium is characterized by the fields

$$N_1(x) = -\bar{q}\,x, \quad M_1(x) = \frac{\lambda L}{8}\mathfrak{g}(x), \quad \alpha_1(x) = \begin{cases} 2, & 0 \le x \le 2.5\,\ell \\ 0, & 2.5\,\ell \le x \le L \end{cases}, \quad \beta(x) = 0, \tag{40}$$

where $\mathfrak{g}$ is the piecewise function linearly interpolating between the three values $\mathfrak{g}(0) = 0$, $\mathfrak{g}(L/2) = 0$ and $\mathfrak{g}(L) = 4$. The fields N_1 and M_1 are plotted in Fig. 11 as dashed black lines. For the equilibria (40) the maximal stress in tension is reached in the point B of coordinates $(x = L, y = h/2)$ where $\sigma = \sigma_B = -\bar{q}L/(bh) + 3\lambda L/(bh^2)$. Equating to the critical value σ_c and solving for λ we obtain a second critical value for the transverse load

$$\lambda_{c2} = \frac{bh^2\sigma_c}{3L} + \frac{\bar{q}h}{3} \simeq 0.8\,\frac{bh^2\sigma_c}{L} > \lambda_{c1}. \tag{41}$$

Hence, the equilibria (40) are stable only for $\lambda \in [\lambda_{c1}, \lambda_{c2})$ and correspond to a cantilever beam where the bending moment due to the transverse force λ is not sufficient to exceed the effects of the compression forces due to $\bar{q}$ in the clamped right end.

[1] Note that with the numerical value chosen for $\bar{q}$, the axial maximum tension $\bar{N}_0 \approx 0.7\,N_c$ is insufficient to independently initiate fracture.

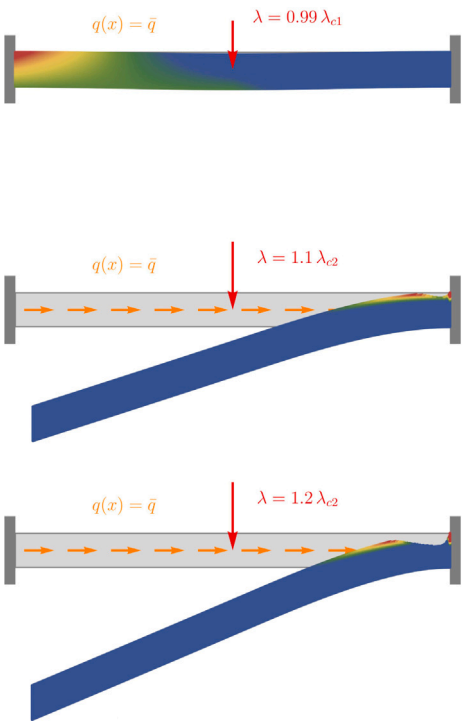

Fig. 10. Evolution of damage and deformed beam shape as the transverse load is increased. The colors refer to the stress magnitude. (For interpretation of the references to color in this figure legend, the reader is referred to the web version of this article.)

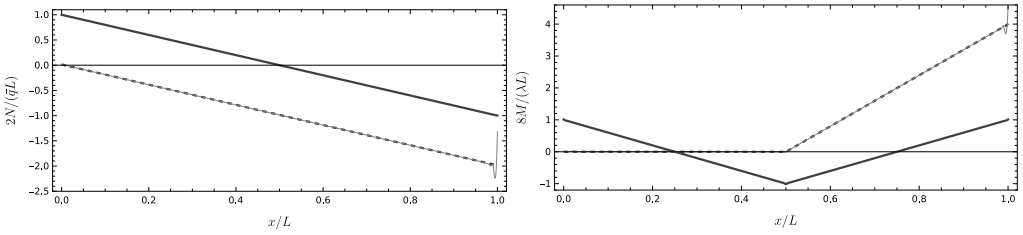

(a) Normalized axial force N. (b) Normalized bending moment M.

Fig. 11. Axial force and bending moment distributions for several value of the transverse force: thick solid lines for $0 < \lambda \in < \lambda_{c1}$, dashed lines for $\lambda_{c1} < \lambda \in < \lambda_{c2}$, thin gray lines for $\lambda > \lambda_{c2}$. These response are computed with the FE code illustrated in Appendix.

For $\lambda \geq \lambda_{c2}$, in order to have $\sigma_B \not> \sigma_c$, the stable equilibrium branch is be characterized by a non vanishing damage of the upper beam surface, *i.e.* $\alpha > 0$ in $x = L$. Indeed, surpassed this second threshold, we numerically observe the emergence of another stable equilibrium branch where the field α near the right end grows from 0 and asymptotically reaches 2 for $\lambda \to \infty$.

In the fracturing of the right end near $x = L$, the damage evolution is continuous with respect to the parameter λ; this is due to the contemporary presence of compression and bending moment. Snapshots of the beam configuration for values of are shown in Fig. 10, whilst the damage distribution α during this last phase is plotted in Fig. 12*a*. Note that the damage profiles for $\lambda \geq \lambda_{c_2}$ near the right end are very similar to the ones found in Fig. 10 of [21] for a cantilever beam; however in their case an initial crack was present at a fixed distance from the clamp. A more detailed explanation of the fracturing process near the right end is reported in the remark below.

We stress the fact that any model neglecting the interaction between axial forces and bending moments would have failed in describing the complex scenario discussed above. Indeed, neglecting the coupling between N and M, we would have predicted the contemporary failures of points A, B, C and an error in the calculation of the critical value λ_{c1} (the decrement from $4/3 \simeq 1.33$ to 0.4 in (39) is due to the presence of the axial load). The computed numerical evolutions with respect to λ for these three beam points are show in Fig. 12*b* by the paths $p_A(\lambda)$ (orange points), $p_B(\lambda)$ (red points) and $p_C(\lambda)$ (brown points) in the plane (N, M).

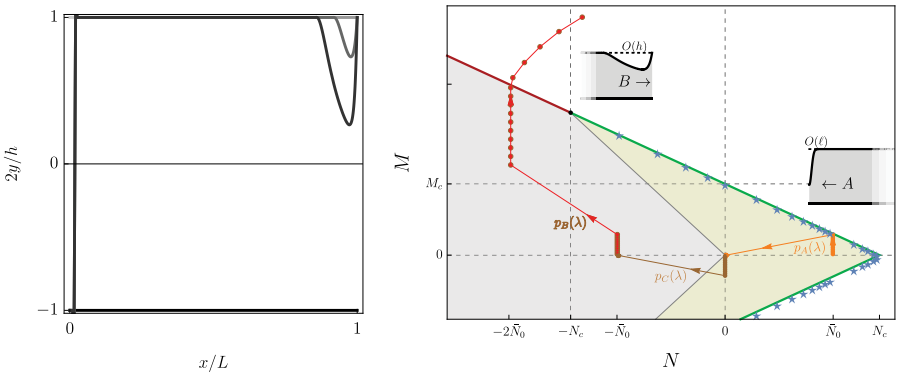

Fig. 12. (a) Damage distributions at several values of the transverse load λ; first a complete fracture at the cross-section in A on the left, then a progressive fracture at the cross section in B. (b) Paths in the stress plane (N, M) for the three beam points A, B and C shown in Fig. 9. The points marked with a star along the boundary of the elastic domain have been numerically determined, solving the problem (23). (For interpretation of the references to color in this figure legend, the reader is referred to the web version of this article.)

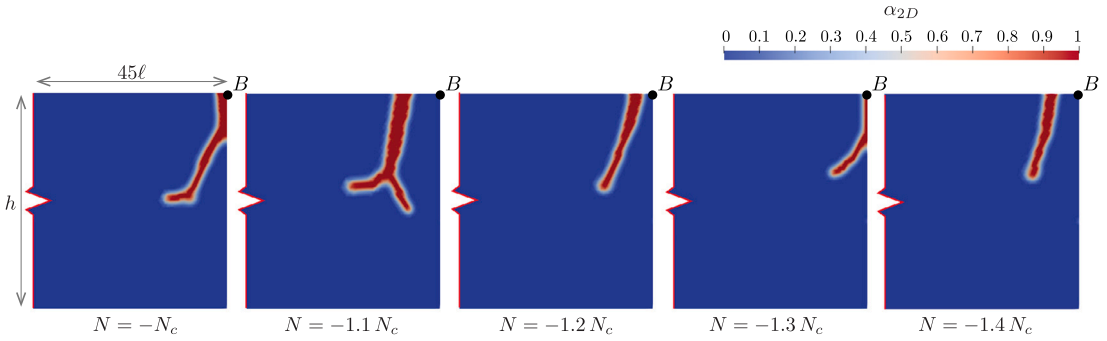

Fig. 13. 2D numerical evidences for the fracture of a cantilever beam-like domain under strong compressions. Zoom of a region in a neighborhood of the point B of Fig. 9.

Remark 3. The Ansatz (7) and the conditions (8) are key in our model. Based on these, when a uniform distribution of N and M is present on a damaged beam, one would naturally expect the maximal value of the stress S_{xx} to correspond to the most eroded cross-section. We show that this is true only for sufficiently small compressive axial forces.

Indeed, assuming without loss of generality $M \geq 0$, using (7) and (12) and imposing a Gaussian localization profile $\alpha = \bar{\alpha}\exp(-\eta\, x^2)$, the stress on the upper surface (for positive bending moments this equals the maximal stress for each section) reads

$$\sigma_u(x) = S_{xx}(x, y = h/2)|_{\alpha(x)=\bar{\alpha}e^{-\eta x^2}} = \frac{4}{(\bar{\alpha}e^{-\eta x^2} - 2)^2 h^2}\left(6M + (\bar{\alpha}e^{-\eta x^2} + 1)hN\right). \tag{42}$$

The condition to have the maximum stress in the "most eroded" point, for the choice made $x = 0$, is independent on the form postulated for the damage profile, is independent of η, depends only on the damage severity $\bar{\alpha}$, M and hN and it reads

$$\sigma_u''(x = 0) < 0 \text{ satisfied when: } 12M + (4 + \bar{\alpha})hN > 0,\ M \geq 0. \tag{43}$$

Therefore, for sufficiently large compressions, $N < -12M/(4 + \bar{\alpha})h$, this condition can be violated and the maximum stress is reached on the sides of the damage profile. When this happens, the damage tends to diffuse and the localization features described in Section 3.3 do not hold anymore.

For $\bar{\alpha} \simeq 0$, condition (43) is violated for $12M + 4hN = 0$ which coincides with the stress-hardening condition of Section 3.2. Therefore, for $N < -N_c$ the damage profile is not anymore localized within a region of size $O(\ell)$. This is exactly the case occurring in point B where the boundary of the elastic domain is reached for $N = -2\bar{N}_0 \simeq -1.4N_c$, see the red path in Fig. 12*b*.

Numerical evidences, based on 2D phase-field simulations, confirm the hardening character for $N < -N_c$ and show that for large compressions, the cracks are not straight but tend to diffuse within the beam domain deviating from the plane $x = L$ and possibly branching, see Fig. 13. Clearly our minimalist model has not sufficient damage descriptors to mimic a similar behavior, hence we interpret the damage diffusion in Fig. 12(a) as a result of this partial descriptive capability.

5. Conclusions and perspectives

This research introduces a novel model damage tailored for planar extensible Euler–Bernoulli beams, integrating several distinctive features. Firstly, we incorporate two phase-field damage parameters to intricately characterize material fracturing, specifically addressing the 'erosion' phenomena occurring both above and below the original, undamaged beam. This dual-parameter approach allows for a more nuanced representation of the fracture process. Secondly, our model assumes a straightforward linear dependency of the axial stress field on the thickness coordinate, accompanied by linear dependence on both axial force and bending moment. This assumption provides simplicity while maintaining a practical representation of the stress distribution within the beam.

Crucially, by adeptly identifying the constitutive response, our model successfully accounts for the coupling between stretching and bending induced during through-the-thickness damage. This interaction is pivotal in accurately capturing the complex behavior of the beam as in the example of Section 4.

Furthermore, our model demonstrates noteworthy agreement with 2D observations, attesting to its efficacy in simulating and predicting the mechanical response of planar Euler–Bernoulli beams subjected to through-the-thickness damage. This robust agreement underscores the model's reliability and its potential applicability in practical scenarios where accurate predictions of structural behavior are essential.

Expanding the scope of our model, we can easily apply it to Kirchhoff–Love plates or Koiter shells. In these cases, the model employs the same two damage parameters to characterize the degradation of both the upper and lower surfaces, along with a linear distribution of membrane stresses throughout the thickness. It is important to note that, given the presence of multiple stress descriptors in various directions, adjustments to the dissipation Eq. (21) are necessary. However, such modifications do not pose a significant challenge.

As highlighted in Section (1), our previous discussion addressed the somewhat limited Ansatz concerning the damage profile. To enhance the accuracy of the model, especially in meeting the boundary conditions within the context of the 3D elasticity problem, a refinement of the damage profile Ansatz could be considered. This refinement would contribute to a more comprehensive representation of the system and ensure a better alignment with the intricacies of the physical problem at hand.

CRediT authorship contribution statement

Giovanni Corsi: Writing – review & editing, Writing – original draft, Software, Formal analysis, Conceptualization. **Antonino Favata:** Writing – review & editing, Writing – original draft, Supervision, Investigation, Formal analysis, Conceptualization. **Stefano Vidoli:** Writing – review & editing, Writing – original draft, Supervision, Investigation, Funding acquisition, Formal analysis, Conceptualization.

Declaration of competing interest

The authors declare that they have no known competing financial interests or personal relationships that could have appeared to influence the work reported in this paper.

Data availability

No data was used for the research described in the article.

Acknowledgments

SV gratefully acknowledges the financial support from the Italian Ministry of University and Research (MUR) in the framework of the Project PRIN 2022: New eco-friendly building materials inspired by ancient constructions (Prot. 2022Y2RHHT). All authors acknowledge the Italian INdAM-GNFM.

Appendix. Details of the FE simulations

The code for both the 1D and 2D numerical simulations has been written in `python` as interface to `FEniCS`, a popular open-source computing platform for solving partial differential equations [25,26]. In particular the package `DOLFIN` [27], a library aimed at automating solution of PDEs using the finite element method, has been used extensively. The repository https://github.com/gcorsi1/EBPhaseField contains all the files to obtain the results shown above.

Specifically, the 2D simulations, see Figs. 2 and 13, use the functional (1) with the splitting proposed [4] in order to not evolve damage under compressive loads. Instead, 1D simulations perform the sequential minimization of the functional (23); here compressive loads are dealt with through a suitable smoothing of the dissipation functions $\hat{c}_i$, and $\check{c}_i$ in (21); to this aim we use the arctan function centered in 0 and $c_\infty = 1000$.

The elastic energy (14) for the damaging Euler–Bernoulli beam (23) contains the transverse displacement field $v \in H^2$; this calls for the use of either C^1 or high-order nonconformal finite-elements. We choose to avoid the difficulties related to their

implementations by using C^0 interior penalty methods (also known as Discontinuous Galërkin methods, see [28]). Following [29], we weakly enforce the continuity of first and higher-order derivatives, rewriting the elastic energy in the form:

$$\mathcal{E} = \frac{1}{2}\int_0^L \left(N\,w' + M\,v''\right)\,\mathrm{d}x - \left[Mv'\right]_0^L + \{\tau_H (v')^2 + \tau_G v^2 + \gamma_G w^2\}_0^L - \int_\Gamma \{M\}[\![v']\!]\mathrm{d}A + \frac{1}{2}\int_\Gamma \tau [\![v']\!]^2 \mathrm{d}A, \tag{A.1}$$

where N and M are given in (18), Γ indicates the inter-element interfaces, $[q]_0^L := q_L - q_0$, $\{q\}_0^L := (q_L + q_0)/2$ and the jump and average operators, $[\![\cdot]\!]$ and $\{\cdot\}$ are defined as usual

$$\{q\} := \frac{1}{2}(q_+ + q_-), \quad [\![q]\!] := q_- - q_+. \tag{A.2}$$

Here the constants τ and τ_H penalize the derivative discontinuities at the interior and outer edges, respectively. The τ_G and γ_G constants are introduced to enforce the Dirichlet boundary conditions in a weak form, a trick that proved important in the numerical example of Section 4, where fracture occurs at one of the beam end points. Optimal choices for the constants τ, τ_H, τ_G and γ_G are the following [29]:

$$\tau = \mathsf{EJ}(0,0)/\delta, \quad \tau_H = 2\mathsf{EJ}(0,0)/\delta, \quad \tau_G = \mathsf{EJ}(0,0)/\delta^3, \quad \gamma_G = \mathsf{EA}(0,0)/\delta, \tag{A.3}$$

with δ the average element size in the mesh. Remark that, while the approach to the DG discretization of the Euler–Bernoulli beam was well known, several new terms are now present in (A.1) due to the presence of the coupling terms between axial force and bending curvatures. Hence, the convergence of the method was not obvious.

As to the material and model parameters, we have chosen: $\mathsf{w}_c = 3G_c/(8\ell) = 0.0375$ N, $\sigma_c = 5.6$ N/m^2, $\nu = 0.3$, $\ell/h = 0.1$, $L/h = 10$, $\ell/\delta = 10$.

References

[1] G. Francfort, J.-J. Marigo, Revisiting brittle fracture as an energy minimization problem, J. Mech. Phys. Solids (ISSN: 0022-5096) 46 (8) (1998) 1319–1342.
[2] L. Ambrosio, V. Tortorelli, Approximation of functional depending on jumps by elliptic functional via *Gamma*-convergence, Comm. Pure Appl. Math. 43 (8) (1990) 999–1036.
[3] B. Bourdin, G. Francfort, J.-J. Marigo, Numerical experiments in revisited brittle fracture, J. Mech. Phys. Solids (ISSN: 0022-5096) 48 (4) (2000) 797–826.
[4] C. Miehe, M. Hofacker, F. Welschinger, A phase field model for rate-independent crack propagation: Robust algorithmic implementation based on operator splits, Comput. Methods Appl. Mech. Engrg. (ISSN: 0045-7825) 199 (45) (2010) 2765–2778.
[5] M. Ambati, T. Gerasimov, L. De Lorenzis, A review on phase-field models of brittle fracture and a new fast hybrid formulation, Comput. Mech. 55 (2) (2015) 383–405.
[6] F. Amiri, D. Millán, Y. Shen, T. Rabczuk, M. Arroyo, Phase-field modeling of fracture in linear thin shells, Theor. Appl. Fract. Mech. (ISSN: 0167-8442) 69 (2014) 102–109, Introducing the new features of Theoretical and Applied Fracture Mechanics through the scientific expertise of the Editorial Board.
[7] L. Weidong, N. Nhon, H. Jiazhao, Z. Kun, Adaptive analysis of crack propagation in thin-shell structures via an isogeometric-meshfree moving least-squares approach, Comput. Methods Appl. Mech. Engrg. (ISSN: 0045-7825) 358 (2020) 112613.
[8] P. Yu-Xiang, Z. A-Man, M. Fu-Ren, A 3D meshfree crack propagation algorithm for the dynamic fracture in arbitrary curved shell, Comput. Methods Appl. Mech. Engrg. (ISSN: 0045-7825) 367 (2020) 113139.
[9] P. Areias, T. Belytschko, Non-linear analysis of shells with arbitrary evolving cracks using XFEM, Internat. J. Numer. Methods Engrg. 62 (3) (2005) 384–415.
[10] J. Dolbow, N. Moës, T. Belytschko, Modeling fracture in Mindlin–Reissner plates with the extended finite element method, Int. J. Solids Struct. (ISSN: 0020-7683) 37 (48) (2000) 7161–7183.
[11] N. Nguyen-Thanh, N. Valizadeh, M. Nguyen, H. Nguyen-Xuan, X. Zhuang, P. Areias, G. Zi, Y. Bazilevs, L. De Lorenzis, T. Rabczuk, An extended isogeometric thin shell analysis based on Kirchhoff-Love theory, Comput. Methods Appl. Mech. Engrg. (ISSN: 0045-7825) 284 (2015) 265–291, Isogeometric Analysis Special Issue.
[12] E. Tanné, T. Li, B. Bourdin, J.-J. Marigo, C. Maurini, Crack nucleation in variational phase-field models of brittle fracture, J. Mech. Phys. Solids 110 (2018) 80–99.
[13] H. Ulmer, M. Hofacker, C. Miehe, Phase field modeling of fracture in plates and shells, PAMM 12 (1) (2012) 171–172.
[14] M. Ambati, L. De Lorenzis, Phase-field modeling of brittle and ductile fracture in shells with isogeometric NURBS-based solid-shell elements, Comput. Methods Appl. Mech. Engrg. 312 (2016) 351–373.
[15] J. Kiendl, M. Ambati, L. De Lorenzis, H. Gomez, A. Reali, Phase-field description of brittle fracture in plates and shells, Comput. Methods Appl. Mech. Engrg. (ISSN: 0045-7825) 312 (2016) 374–394, Phase Field Approaches to Fracture.
[16] K. Paul, C. Zimmermann, K. Mandadapu, T. Hughes, C. Landis, R. Sauer, An adaptive space-time phase field formulation for dynamic fracture of brittle shells based on LR NURBS, Comput. Mech. 65 (2020) 1039–10623.
[17] D. Proserpio, M. Ambati, L. De Lorenzis, J. Kiendl, A framework for efficient isogeometric computations of phase-field brittle fracture in multipatch shell structures, Comput. Methods Appl. Mech. Engrg. (ISSN: 0045-7825) 372 (2020) 113363.
[18] G. Kikis, M. Ambati, L. De Lorenzis, S. Klinkel, Phase-field model of brittle fracture in Reissner–Mindlin plates and shells, Comput. Methods Appl. Mech. Engrg. (ISSN: 0045-7825) 373 (2021) 113490.
[19] G. Corsi, A. Favata, S. Vidoli, A coarse-grained constitutive law for fracturing beams based on a sharp interface crack representation, Int. J. Solids Struct. 269 (2023) 112224.
[20] G. Corsi, A. Favata, S. Vidoli, A phase-field model for fracture in beams from asymptotic results in 2D elasticity, Mater. Res. Proc. (2023).
[21] W. Lai, G. J., Y. Li, M. Arroyo, Y. Shen, Phase field modeling of brittle fracture in an Euler-Bernoulli beam accounting for transverse part-through cracks, Comput. Methods Appl. Mech. Engrg. 361 (2020) 112787.
[22] B. Halphen, Q. Nguyen, Sur les matériaux standards généralisés, J. Mec. 14 (1975) 39–63.
[23] A. Mielke, Evolution of Rate-Independent Systems, North-Holland, Amsterdam, 2005, pp. 461–559.
[24] K. Pham, J. Marigo, From the onset of damage to rupture: construction of responses with damage localization for a general class of gradient damage models, Contin. Mech. Thermodyn. 25 (2013) 147–171.
[25] M.S. Aln, B. Kehlet, A. Logg, C. Richardson, J. Ring, E. Rognes, G. Wells, The FEniCS project version 1.5, 2015, p. 15.
[26] A. Logg, K. Mardal, G. Wells (Eds.), Automated Solution of Differential Equations by the Finite Element Method, in: Lecture Notes in Computational Science and Engineering, vol. 84, Springer Berlin Heidelberg, 2012, ISBN: 978-3-642-23098-1 978-3-642-23099-8.

[27] A. Logg, G. Wells, DOLFIN, ACM Trans. Math. Software 37 (2) (2010) 1–28.
[28] D. Arnold, F. Brezzi, B. Cockburn, D. Marini, Discontinuous Galerkin methods for elliptic problems, in: B. Cockburn, G.E. Karniadakis, C.-W. Shu (Eds.), Discontinuous Galerkin Methods, Springer Berlin Heidelberg, Berlin, Heidelberg, ISBN: 978-3-642-59721-3, 2000, pp. 89–101.
[29] G. Engel, K. Garikipati, T. Hughes, M. Larson, L. Mazzei, R. Taylor, Continuous/discontinuous finite element approximations of fourth-order elliptic problems in structural and continuum mechanics with applications to thin beams and plates, and strain gradient elasticity, Comput. Methods Appl. Mech. Engrg. 191 (34) (2002) 3669–3750.